

EchoIR: Advancing Image Restoration with Echo Upsampling and Bi-Level Optimization

Yuhan He¹, Yuchun He¹

¹University of Sydney
Camperdown NSW 2050, Australia
{yuhe0760, yuhe0953}@uni.sydney.edu.au

Abstract

Image restoration represents a fundamental challenge in low-level vision, focusing on reconstructing high-quality images from their degraded counterparts. With the rapid advancement of deep learning technologies, transformer-based methods with pyramid structures have advanced the field by capturing long-range cross-scale spatial interaction. Despite its popularity, the degradation of essential features during the upsampling process notably compromised the restoration performance, resulting in suboptimal reconstruction outcomes. We introduce the EchoIR, an UNet-like image restoration network with a bilateral learnable upsampling mechanism to bridge this gap. Specifically, we proposed the Echo-Upsampler that optimizes the upsampling process by learning from the bilateral intermediate features of U-Net, the "Echo", aiming for a more refined restoration by minimizing the degradation during upsampling. In pursuit of modeling a hierarchical model of image restoration and upsampling tasks, we propose the Approximated Sequential Bi-level Optimization (AS-BLO), an advanced bi-level optimization model establishing a relationship between upsampling learning and image restoration tasks. Extensive experiments against the state-of-the-art (SOTA) methods demonstrate the proposed EchoIR surpasses the existing methods, achieving SOTA performance in image restoration tasks.

Introduction

Image restoration stands as a fundamental image-processing task to reconstruct high-quality images from their degraded counterparts (Li et al. 2025, 2023; Jiang et al. 2024; Zou et al. 2024b,a). However, the challenge of image restoration primarily stems from the loss or absence of information inherent in the input image, such as noise and blur, which can obscure essential image details. Effectively distinguishing between image degradation and the main information of the image, and subsequently restoring the lost information, has become a formidable problem. With the rise of deep learning, researchers began exploring its applications in image-related tasks. Convolutional Neural Networks (CNN) (LeCun, Bengio, and Hinton 2015) introduced new methods for image restoration (Ren et al. 2021; Zhang et al. 2019). However, CNNs have limited capability in capturing long-range dependencies on pixel information, restricting their

Copyright © 2025, Association for the Advancement of Artificial Intelligence (www.aaai.org). All rights reserved.

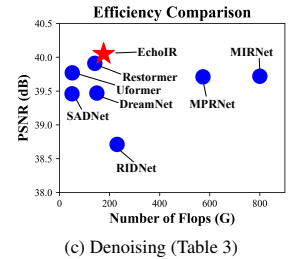
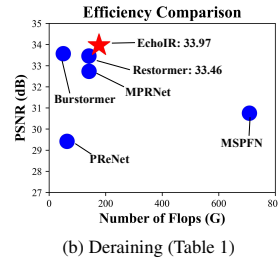
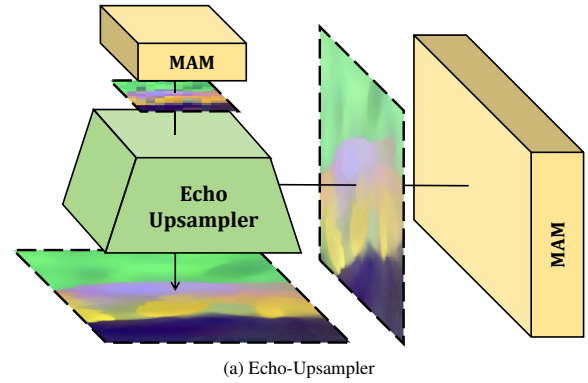


Figure 1: Schematic diagram of the Echo-Upsampler and comparison of the EchoIR model with other methods in deraining and denoising tasks. MAM is Mix-attention module.

effectiveness. Transformers establish feature dependencies through attention mechanisms, leading to promising results in visual tasks (Liang et al. 2021; Zamir et al. 2021). Despite this, Transformers suffer from quadratic growth in computational complexity with increasing spatial resolution. To improve efficiency, solutions such as spatial window attention and combining multiple attention mechanisms have been proposed (Zhang et al. 2022b; Chen et al. 2023b).

Existing image restoration methods often face challenges with information loss during downsampling, leading to inadequate upsampling and poor restoration outcomes. Downsampling reduces feature map size, losing crucial information and impacting recovery. Although U-Net (Ronneberger, Fischer, and Brox 2015; Zamir et al. 2022, 2021) and ResNet (He et al. 2016; Liang et al. 2021; Zhang et al. 2022b; Chen et al. 2023b) structures help retain features, the retained in-

formation is often insufficient.

To address the aforementioned challenges, we propose EchoIR, a bilaterally learnable upsampling image restoration network built upon the U-Net architecture. We refer to the feature information obtained during the U-Net downsampling process as "echo", which is subsequently utilized during the upsampling phase. Specifically, we introduce the Echo-Upsampler, which learns the upsampling process by leveraging the "echo" derived from U-Net downsampling encoding, thereby enhancing the quality of upsampling.

To enhance the image restoration and upsampling tasks, we introduce a hyperparameter optimization strategy to simplify the bi-layer optimization model. This strategy breaks down the complex Echo-Upsampler and image restoration optimization into single-layer problems solvable via gradient descent. Our proposed Approximated Sequential Bi-level Optimization (AS-BLO) reformulates the complex bi-level model into non-constraint single-level tasks, which are easier to solve by gradient descent, and proves the asymptotic convergence of these approximated problems.

By employing Echo-Upsampler and AS-BLO, we efficiently preserve nuanced features, thereby enhancing the quality of upsampling and image restoration. Additionally, our proposed hyperparameter optimization strategy for reformulating the bi-level optimization model ensures the execution of an optimal upsampling process and minimizes image recovery loss. Our contributions are as follows:

- To address the issue of image information loss during the upsampling process in existing methods, we introduce the Echo-Upsampler. This component optimizes the upsampling procedure by learning from the bilateral intermediate features of U-Net.
- We proposed the Approximated Sequential Bi-level Optimization (AS-BLO) to model the problems of image restoration and Echo-Upsampler learning. By transforming it into a sequential single-layer optimization problem, we solve the original complex hierarchical model using gradient descent.
- Extensive experiments prove that the proposed Echo-Net achieves state-of-the-art (SOTA) recovery results in the image denoising, deraining, and deblurring tasks.

Related Work

Image Restoration

The field of image restoration has experienced a transformation with the integration of deep learning technologies. Denoising, deblurring, and deraining are three essential tasks in the field of image restoration. Denoising involves the removal of noise from images. Noise can occur due to various factors, including sensor imperfections, environmental conditions during the image capture process, or data transmission errors. The objective of denoising models (Zuo, Zhang, and Zhang 2018; Zamir et al. 2022) is to recover the original, clean image by eliminating this noise while preserving important details and structures. Deblurring is the process of removing blur from images. Blur can be caused by several factors, such as camera or subject movement during exposure, out-of-focus shooting, or atmospheric disturbances.

Deblurring models (Wang et al. 2022; Tsai et al. 2022) aim to sharpen the image details that have been smeared or obscured due to blur, restoring clarity and improving the overall image quality. Deraining removes rain streaks or droplets that degrade image quality. Deraining methods (Chen et al. 2021; Zamir et al. 2022) enhance visual appeal and usability by eliminating these artifacts. Among the trailblazing models that have set the foundation for these advancements, SRCNN (Dong et al. 2014) and ARCNN (Yu et al. 2016) stand out as pioneering efforts in applying convolutional neural networks (CNNs) for image restoration tasks.

Transformer-based Restoration

These initial models laid the groundwork for subsequent advancements by incorporating sophisticated CNN architectures and techniques like residual connections (Cavigelli, Hager, and Benini 2017; Kim, Lee, and Lee 2016; Zhang et al. 2022a). However, CNN-based methods often struggle with modeling global dependencies effectively. Generative adversarial networks (GANs) (Gulrajani et al. 2017; Wang et al. 2018) have also been used for image restoration but face challenges such as mode collapse, difficult training processes, and potential inaccuracies, leading to ongoing research for improvements.

These challenges have spurred the exploration of Transformers as a powerful alternative due to their ability to capture global dependencies effectively. Initially applied in natural language processing, Transformers (Vaswani et al. 2017) have proven effective in computer vision through models like Vision Transformer (ViT) (Dosovitskiy et al. 2021). Despite their strengths, Transformers in image restoration, such as IPT (Chen et al. 2021) and SwinIR (Liang et al. 2021), face challenges with quadratic computational complexity in their self-attention mechanisms. IPT tackles this by processing smaller image patches independently, while SwinIR uses shifted window attention for enhanced performance. Further advancements (Chen et al. 2023a, 2024, 2023c; Li et al. 2022b; Zamir et al. 2022) have been made in developing effective attention mechanisms for restoration. However, current methods have not effectively addressed the issue of information loss during upsampling.

Method

The architectural framework of EchoIR is delineated in Figure 2, comprising four principal components: shallow feature extraction, feature encoder, feature decoder, and image reconstruction. Shallow feature extraction entails acquiring multi-channel feature maps through convolutional operations. The feature encoder integrates mix-attention modules and downsamplers to facilitate deep feature extraction across different levels. Each mix-attention module encompasses multiple mix-attention blocks to enable deep feature extraction at every level. The feature decoder employs Mix-Attention modules and Echo-Upsamplers to execute feature extraction and restore the feature map to the dimensions of shallow features. The Echo-Upsampler expands the current features guided by the encoder layer features. Leveraging the AS-BLO optimization method enhances the training of

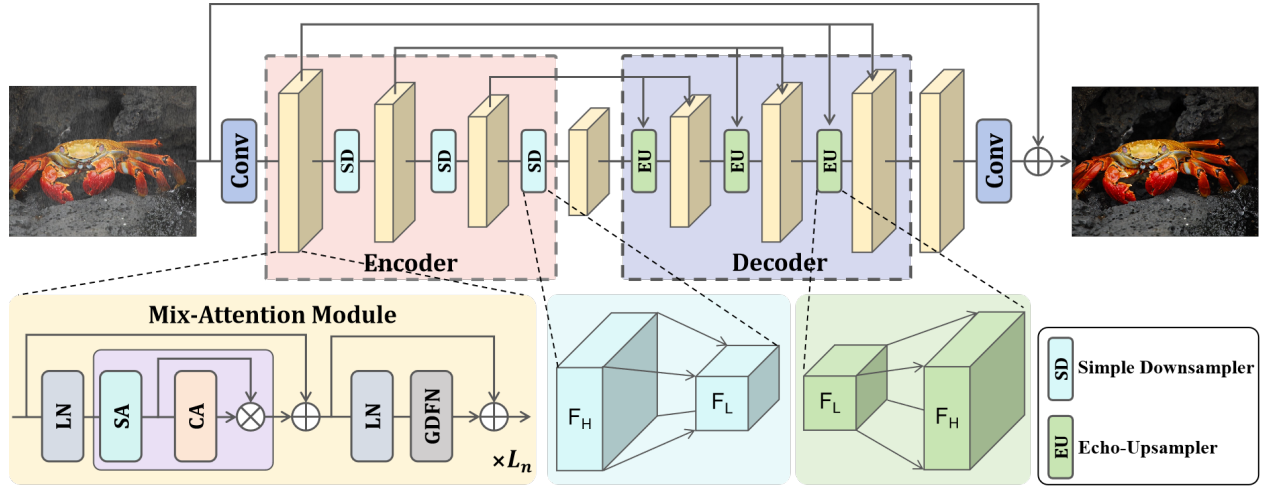


Figure 2: The structure of EchoIR. SD is the simple downsampler. EU is Echo-upsampler. LN is layer normalization, SA is multi-head self-attention, CA is channel attention, and GDFN is gated-Dconv FN.

the upper echo sampler. Ultimately, image reconstruction transpires to convert feature maps into restored images.

Overall Architecture

Given a low-quality image $I_L \in \mathbb{R}^{3 \times H \times W}$ (H is the height of the image, W is the width of the image), EchoIR first generates a feature map $F \in \mathbb{R}^{C \times H \times W}$ by shallow feature extraction. The feature encoder processes the feature map by a series of mix-attention modules (MAM) with length $[L_1, L_2, \dots, L_n]$. The shape of the feature map before and after each MAM remains consistent. After a MAM processes the feature map, it goes through a simple downsampler, and its height and width will be half of the original, and the number of channels will be doubled. After passing through the feature encoder, the feature map becomes $F_e \in \mathbb{R}^{2C \times \frac{H}{2} \times \frac{W}{2}}$. After a middle block, the feature map is passed to the decoder. The feature decoder also uses the same numbers of MAMs as the encoder to process the feature map. The lengths of the models are $[L_n, L_{n-1}, \dots, L_1]$. Except for the last MAM, the feature map passes through an Echo-Upsampler before entering the MAM. The Echo-Upsampler will double the height and width of the feature map and reduce the number of channels to half. The feature map after the feature decoder is $F_d \in \mathbb{R}^{C \times H \times W}$.

Mix-Attention Block

Compared with the general attention structure, mix-attention combines channel attention and multi-head self-attention. The feature map F_t is first subjected to layer normalization when entering the Mix-attention Block. During the multi-head self-attention process, F_t undergoes a convolution operation to triple the number of channels. Divide the F_t into three parts, Q, K, and V, and divide these three parts into

multiple heads. Do the following for Q, K, and V:

$$\text{Alpha}(Q, K) = \frac{(Q \cdot K)}{\sqrt{d}},$$

$$\text{Attention}(Q, K, V) = V \cdot \text{Softmax}(\text{Alpha}(Q, K)). \quad (1)$$

After multi-head self-attention, the Mix-attention Block gets F_{ts} and enters the channel attention process.

F_{ts} first obtains a one-dimensional feature $pw \in \mathbb{R}^C$ through adaptive average pooling. pw gets $cw \in \mathbb{R}^C$ after passing through a multi-layer perceptron and Sigmoid heuristic function. Perform element-level multiplication of feature maps F_{ts} and cw to obtain F_{tc} . Perform element-level addition of F_{tc} and F_t to obtain F_{ta} . The process is shown as:

$$\begin{aligned} pw &= \text{AdaptiveAvgPool}(F_{ts}), \\ cw &= \text{Sigmoid}(\text{Mlp}(pw)), \\ F_{tc} &= F_{ts} \otimes cw, \quad F_{ta} = F_{tc} \oplus F_t. \end{aligned} \quad (2)$$

Then F_{ta} undergoes layer normalization and gated-Dconv FN (GDFN) (Zamir et al. 2022) to obtain F_{tg} . GDFN can be used to filter effective information for further feature extraction. Perform element-level addition of F_{tg} and F_{ta} to obtain F_{t+1} . F_{t+1} will enter the next Mix-attention Block or other modules.

$$\begin{aligned} pw &= \text{AdaptiveAvgPool}(F_{ts}), \\ cw &= \text{Sigmoid}(\text{Mlp}(pw)), \\ F_{tc} &= F_{ts} \otimes cw. \end{aligned} \quad (3)$$

Echo-Upsampler

During the upsampling process, the Echo-Upsampler uses the output features of the Mix-attention module at the same level in the encoder as a reference to perform the upsampling operation. It is similar to joint bilateral upsampling (JBU)

(Kopf et al. 2007). JBU can produce smoother and higher-resolution results with fewer parameters. The reference input in Echo-Unpsampler is a feature map but not a high-quality image. The workflow of the Echo-Unpsampler is shown in figure 1. The process is as follows:

$$W(p, p') = f(p, p') \oplus g(F_{ref}[p], F_{ref}[p']),$$

$$F_{up}[p] = \frac{1}{\text{sum}(W(p, p'))} \sum_{p' \in \Omega} F_{down}[p'] \cdot W(p, p'). \quad (4)$$

F_{down} is the feature map before upsample, and F_{up} is after upsample. F_{ref} is the referenced feature map from the Mix-Attention Modules in the encoder. Different Echo-upsamplers use the feature map of the corresponding level of the encoder as a reference. Ω is a set of pixels within a certain range centered on pixel p . f and g represent two filter kernels: spatial kernel and range kernel. f is a Gaussian kernel which is shown as:

$$f(p, p') = e^{-\frac{\|p-p'\|^2}{2\sigma^2}}. \quad (5)$$

where parameter σ is learnable. g is also calculated using the Gaussian kernel function. Since F_{ref} is not a high-definition lossless image, a multi-layer perceptron is added on this basis to adjust F_{ref} . The process is shown as:

$$g(F_{ref}[p], F_{ref}[p']) = e^{-\frac{\|Mlp(F_{ref}[p]) - Mlp(F_{ref}[p'])\|^2}{2\sigma^2}}. \quad (6)$$

Through this sampling method, a higher-quality output can be obtained when the input features are not smooth enough. This is beneficial to the subsequent Mix-Attention module for feature extraction.

Approximated Sequential Bi-Level Optimization

Our network is architected to optimize image reconstruction as its upper-level (UL) goal while taking image restoration and a lossless Echo-Unpsampler as foundational lower-level (LL) objectives. This configuration forms a hierarchical bi-level optimization framework, where the UL objective synergizes with the LL solutions to enhance the overall reconstruction quality:

$$\min_{\beta \in \mathcal{B}} \min_{\omega \in \mathbb{R}^n} F(\beta, \omega; \mathcal{D}_{val}),$$

$$\text{s.t. } \omega \in \mathcal{S}(\beta) := \arg \min_{\omega} f(\beta, \omega; \mathcal{D}_{tr}), \quad (7)$$

where β is the UL hyperparameter, ω is the LL parameter. $\mathcal{S}(\beta)$ is the solution set of the LL objective. The notations $F(\cdot)$ and $f(\cdot)$ correspond to the objectives of the UL and LL, respectively. The datasets \mathcal{D}_{val} and \mathcal{D}_{tr} delineate the distinct sets of data reserved for validation and training purposes, respectively. To solve the LL convexity assumption and the possible non-singleton $\mathcal{S}(\beta)$, we transform the complex bi-level optimization model in Eq. 7 into a concise version:

$$\min_{\beta \in \mathcal{B}} \varphi(\beta; \mathcal{D}_{val}),$$

$$\varphi(\beta; \mathcal{D}_{val}) := \min_{\omega} \{F(\beta, \omega; \mathcal{D}_{val}) : \omega \in \mathcal{S}(\beta)\}, \quad (8)$$

where $\varphi(\cdot)$ is the value-function of the LL objective. For a fixed β , solving $\varphi(\cdot)$ is a tractable bi-level optimization

problem with one variable ω . We simplify it further to a series of single-level problems using the value function of the LL problem:

$$f^*(\beta; \mathcal{D}_{tr}) := \min_{\omega} f(\beta, \omega; \mathcal{D}_{tr}). \quad (9)$$

Then the model can be further reformulated as:

$$\varphi(\beta; \mathcal{D}_{val}) =$$

$$\min_{\omega} \{F(\beta, \omega; \mathcal{D}_{val}) : f(\beta, \omega; \mathcal{D}_{tr}) \leq f^*(\beta; \mathcal{D}_{tr})\}. \quad (10)$$

We then add a barrier function and a regularization term $\frac{\mu}{2}\|\omega\|^2$, $\mu > 0$, reformulating the model as follows:

$$\varphi_{\mu, \theta, \sigma}(\beta; \mathcal{D}_{val}) =$$

$$\min_{\omega} \left\{ F(\beta, \omega; \mathcal{D}_{val}) + P_{\sigma}(\beta, \omega; \mathcal{D}_{tr}) + \frac{\theta}{2}\|\omega\|^2 \right\}, \quad (11)$$

$$P(\zeta; \sigma) = \begin{cases} -\sigma(\log(-\zeta) + \eta_1), & -\kappa \leq \zeta < 0 \\ -\sigma\left(\eta_2 + \frac{\eta_3}{\zeta^2} + \frac{\eta_4}{\zeta}\right), & \zeta < -\kappa \\ \infty, & \zeta \geq 0 \end{cases} \quad (12)$$

where in Eq. 11, the $P_{\sigma}(\beta, \omega; \mathcal{D}_{tr})$ denoted as $P_{\sigma}(f(\beta, \omega; \mathcal{D}_{tr}) - f^*(\beta; \mathcal{D}_{tr}))$ is the barrier function with parameter σ for sequential unconstrained minimization. $0 < \kappa \leq 1$, $\eta_1, \eta_2, \eta_3, \eta_4$ are chosen such that $P_{\sigma} \geq 0$ and is twice differentiable. $\frac{\theta}{2}\|\omega\|^2$ stands for the regularization term and $(\mu, \theta, \sigma) > 0$. This reformulates the constraint problem in Eq. 10 into a sequence of unconstrained converge single-level problems.

Recall that the $\omega \in \mathcal{S}(\beta)$ is unique, denote as $\omega^*(\beta)$, then the approximated $\nabla_{\beta} \varphi(\beta; \mathcal{D}_{val})$ is calculated by chain rule:

$$\nabla_{\beta} \varphi(\beta; \mathcal{D}_{val}) = \nabla_{\beta} F(\beta, \omega^*; \mathcal{D}_{val}) + G(\beta),$$

$$\text{s.t. } G(\beta) = (\nabla_{\beta} \omega^*)^T \cdot \nabla_{\omega} F(\beta, \omega^*; \mathcal{D}_{val}), \quad (13)$$

where the $\nabla_{\beta} F(\beta, \omega^*; \mathcal{D}_{val})$ is explicit gradient, $G(\beta)$ is implicit gradient, so only $G(\beta)$ is what we after to solve. We denote:

$$\mathbf{z}_{\mu}^*(\beta) = \arg \min_{\omega} \left\{ f(\beta, \omega; \mathcal{D}_{tr}) + \frac{\mu}{2}\|\omega\|^2 \right\}, \quad (14)$$

$$\omega_{\mu, \theta, \sigma}^*(\beta) =$$

$$\arg \min_{\omega} \left\{ F(\beta, \omega; \mathcal{D}_{val}) + P_{\sigma}(\beta, \omega; \mathcal{D}_{tr}) + \frac{\theta}{2}\|\omega\|^2 \right\}, \quad (15)$$

where the $P_{\sigma}(\cdot)$ in Eq. 15 stands for $P_{\sigma}(f(\beta, \omega; \mathcal{D}_{tr}) - f^*(\beta; \mathcal{D}_{tr}))$. Given $\beta \in \mathcal{B}$, and $\mu, \theta, \sigma > 0$, $\mathbf{z}_{\mu}^*(\beta)$ and $\omega_{\mu, \theta, \sigma}^*(\beta)$ are singleton, we then have $\varphi_{\mu, \theta, \sigma}(\beta; \mathcal{D}_{val})$ differentiable and $G(\beta)$ can be solved:

$$G(\mathbf{x}) = \nabla_{\beta} P_{\sigma}(f(\beta, \omega; \mathcal{D}_{tr}) - f^*(\beta; \mathcal{D}_{tr}))|_{\omega=\omega_{\mu, \theta, \sigma}^*(\beta)}, \quad (16)$$

where $f_{\mu}^*(\beta; \mathcal{D}_{tr}) = f(\beta, \mathbf{z}_{\mu}^*(\beta); \mathcal{D}_{tr}) + \frac{\mu}{2}\|\mathbf{z}_{\mu}^*(\beta)\|^2$ and $\nabla_{\beta} f_{\mu}^*(\beta; \mathcal{D}_{tr}) = \nabla_{\beta} f_{\mu}^*(\beta, \omega; \mathcal{D}_{tr})|_{\omega=\mathbf{z}_{\mu}^*(\beta)}$. Since we have $f(\beta, \omega; \mathcal{D}_{tr})$ is level-bounded in ω locally uniformly in $\beta \in \mathcal{B}$, the inf-compactness condition holds for $f(\cdot) + \frac{\mu}{2}\|\omega\|^2$.

Experiments

Experiments Setting

For the structure of EchoIR in this experiment, the lengths of the Mix-Attention modules in the encoder are 4, 6, and 6 respectively, and the feature map dimensions for each module are 48, 96, and 192. The structure of the decoder is the same as that of the encoder but in reverse order. The length of the module in the middle block is 8, and the dimension of the feature map is 384. The final processing module length is 4, and the feature map dimension is 48. The expansion factor of GDFN is 2.66. In the experiment, the number of iterations is $3e+5$. The stages of iterations are divided into [92000, 64000, 48000, 36000, 36000, 24000], the corresponding patch size is [144, 160, 192, 224, 320, 336] and the batch size is [6, 5, 4, 2, 1, 1]. The initial learning rate of training is $3e-4$. The learning rate begins to decrease gradually after 92,000 iterations until it finally drops to $1e-6$. The GPU in experiments is V100-32GB. Some contrasting methods such as Restormer and Burstormer were retrained.

Deraining Results

The experiment validates the training outcomes of our model using four benchmark datasets: Test100 (Zhang, Sindagi, and Patel 2019), Rain100H (Yang et al. 2017), Rain100L, Test2800 (Fu et al. 2017b), and Test1200 (Zhang and Patel 2018). As depicted in Table 1, our model exhibits remarkable performance across all datasets. Among all datasets, our model demonstrates the highest PSNR performance on the Test100 dataset, surpassing the second-best model by 0.45 dB. Additionally, it achieves the best SSIM performance on the Test1200 dataset, exceeding the second place by 0.015.

The experiment also entailed a visual comparison of the deraining task, as depicted in Figure 3. DGUNet and MPRNet struggle to effectively remove rain and fog. While MFDNet and PReNet manage to eliminate most rain, residual noise from the precipitation remains in some images. Restormer, while successful in rain removal, exhibits noticeable texture and color loss, particularly on the door surface. The results of EchoIR closely resemble ground truth, with rain cleanly removed, showcasing the effectiveness of EchoIR in rain removal tasks.

Deblurring Results

The experiment validates the training outcomes of our model using four benchmark datasets: GoPro (Nah, Hyun Kim, and Mu Lee 2017), HIDE (Shen et al. 2019), RealBlur-R (Rim et al. 2020), and RealBlur-J (Rim et al. 2020). As depicted in Table 2, our model exhibits remarkable performance across all datasets. With the exception of the performance on the GoPro dataset, where it lags behind Stripformer, EchoIR exhibits the highest PSNR and SSIM performance. Particularly noteworthy is our model’s superior performance on the RealBlur-R dataset, with PSNR and SSIM values exceeding the second-highest results by 0.13dB and 0.003, respectively. This underscores the efficacy of our model’s feature extraction capabilities in the realm of image restoration.

The experiment further assessed the visual performance of the model results to facilitate a more intuitive compari-

son between models. Figure 4 illustrates the image details of the model output. In the original blurry image, the text on the truck compartment is notably indistinct and barely discernible, while the boundary between the white car’s roof and the truck appears blurred as well. In the restored results, various methods exhibit different degrees of restoration. For instance, MIMO-Unet+ effectively enhances the clarity of the text but struggles with the blurriness between the car roof and the text. On the other hand, models like Restormer and Stripformer manage to restore the relationship between the car roof and the text, yet the text remains somewhat blurred. In contrast, our model excels in both aspects simultaneously. This indicates that our model demonstrates a more comprehensive feature extraction capability, allowing it to effectively utilize features for image restoration.

Denosing Results

In the denosing experiment, emphasis was placed on real image denosing tasks, with verification conducted on datasets such as SIDD (Abdelhamed, Lin, and Brown 2018) and DND (Plotz and Roth 2017). As demonstrated in Table 3, our method exhibits exceptional metric performance across both datasets. This indicates that the images generated by our model closely resemble the ground truth results, highlighting the model’s accuracy in noise removal and information restoration tasks in denosing.

For the visual comparison of the denosing task, we utilize the difference map between the denosing results and the ground truth to enhance the contrast effect. In this representation, more blue areas signify smaller differences, while more green or red areas indicate greater disparities. As illustrated in the results depicted in Figure 5, other methods exhibit a noticeable presence of green areas in the comparison between the two groups. Conversely, our method outperforms others in both sets of difference maps, with the blue portion occupying the largest proportion and appearing the deepest. This suggests that the denosing results generated by our model closely resemble the ground truth. Additionally, this underscores the efficacy of our model’s feature extraction approach in denosing tasks.

Ablation Study

The experiment setting of the ablation study is the same as the complete experiment except the number of iterations was reduced to $1e+5$. Experiments compare PSNR, SIMM, and FLOPs. Ablation experiments examine the necessity of the Echo Upsampler, AS-BLO, and Mix-Attention blocks.

Echo-Upsampler. The task for the ablation experiment of the Echo-Upsampler is single-image deraining. We first replace it with a simple upsampler to compare the effect. A simple upsampler consists of a convolutional layer and a pixel shuffle. For the test of the Echo-Upsampler, we changed its reference object to the input image I_L instead of feature maps from the encoder. The experimental results are shown in Table 4. From the experimental results, the best results can be achieved by using an Echo-Upsampler and using encoder feature maps of different levels as reference input.

Mix-Attention block. The task of the ablation experiment of the Mix-Attention block is denosing. In the ex-

Table 1: Comparison with the deraining methods. The best result is in red and the second one is in blue.

Methods	Test100		Rain100H		Rain100L		Test2800		Test1200		Average	
	PSNR↑	SSIM↑	PSNR↑	SSIM↑	PSNR↑	SSIM↑	PSNR↑	SSIM↑	PSNR↑	SSIM↑	PSNR↑	SSIM↑
DerainNet (Fu et al. 2017a)	22.77	0.810	14.92	0.592	27.03	0.884	24.31	0.861	23.38	0.835	22.48	0.796
SEMI (Wei et al. 2019)	22.35	0.788	16.56	0.486	25.03	0.842	24.43	0.782	26.05	0.822	22.88	0.744
PReNet (Ren et al. 2019)	24.81	0.851	26.77	0.858	32.44	0.950	31.75	0.916	31.36	0.911	29.42	0.897
MSPFN (Jiang et al. 2020)	27.50	0.876	28.66	0.860	32.40	0.933	32.82	0.930	32.39	0.916	30.75	0.903
MPRNet (Zamir et al. 2021)	30.27	0.897	30.41	0.890	36.40	0.965	33.64	0.938	32.91	0.916	32.73	0.921
MFDNet (Wang et al. 2023)	30.78	0.914	30.48	0.899	37.61	0.973	33.55	0.939	33.01	0.925	33.08	0.930
DGUNet (Mou, Wang, and Zhang 2022)	30.32	0.899	30.66	0.891	37.42	0.969	33.68	0.938	33.23	0.920	33.06	0.923
SPAIR (Purohit et al. 2021)	30.35	0.909	30.95	0.892	36.93	0.969	33.34	0.936	33.04	0.922	32.91	0.926
Restormer (Zamir et al. 2022)	31.63	0.923	31.14	0.907	37.46	0.972	33.98	0.942	33.11	0.926	33.46	0.934
Burstormer (Dudhane et al. 2023)	31.72	0.930	31.20	0.911	37.59	0.982	34.09	0.949	33.25	0.932	33.57	0.941
EchoIR (ours)	32.17	0.939	31.58	0.926	38.04	0.993	34.41	0.953	33.66	0.947	33.97	0.952

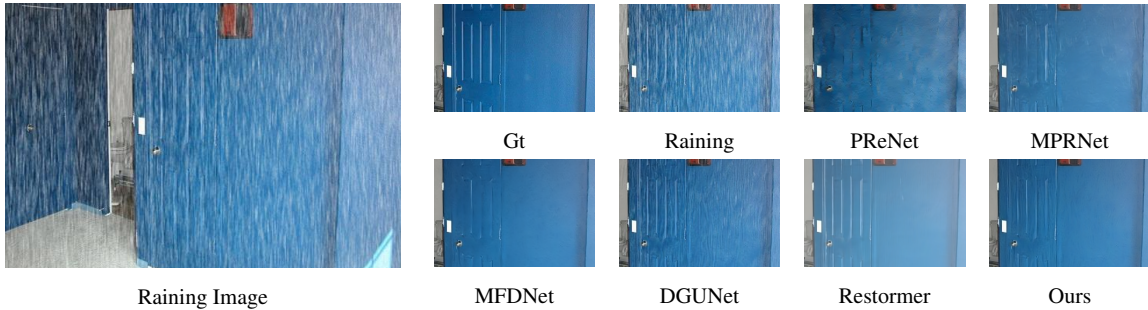


Figure 3: Visual comparison of results with SOTA draining methods. This comparison employs the output results for direct comparison, thereby providing a clear reflection of the quality of the model’s output outcomes.

Table 2: Quantitative comparison with the SOTA deblurring methods. The best result is in red and the second best one is in blue. The comparison methods include DeblurGAN (Kupyn et al. 2018), DeblurGAN-v2 (Kupyn et al. 2019), SRN (Tao et al. 2018), DBGAN (Zhang et al. 2020), MT-RNN (Park et al. 2020), DMPHN (Zhang et al. 2019), MIMO-Unet+ (Cho et al. 2021), MPRNet, Restormer, and Stripformer (Tsai et al. 2022).

Methods	GoPro		HIDE		RealBlur-R		RealBlur-J	
	PSNR↑	SSIM↑	PSNR↑	SSIM↑	PSNR↑	SSIM↑	PSNR↑	SSIM↑
DeblurGAN	28.70	0.858	24.51	0.871	33.79	0.903	27.97	0.834
DeblurGAN-v2	29.55	0.934	26.61	0.875	35.26	0.944	28.70	0.866
SRN	30.26	0.934	28.36	0.915	35.66	0.947	28.56	0.867
DBGAN	31.10	0.942	28.94	0.915	33.78	0.909	24.93	0.745
MT-RNN	31.15	0.945	29.15	0.918	35.79	0.951	28.44	0.862
DMPHN	31.20	0.940	29.09	0.924	35.70	0.948	28.42	0.860
MIMO-Unet+	32.45	0.957	29.99	0.930	35.54	0.947	27.63	0.837
MPRNet	32.66	0.959	30.96	0.939	35.99	0.952	28.70	0.873
Restormer	32.67	0.960	31.09	0.942	36.08	0.955	28.83	0.875
Stripformer	33.08	0.962	31.03	0.940	36.02	0.954	28.89	0.877
EchoIR (ours)	32.82	0.962	31.18	0.948	36.21	0.958	28.94	0.880

periment of the Mix-Attention block, we first ablated the channel attention part and only retained the multi-head self-attention in the attention calculation. We then ablated GDFN and replaced FFN with a multi-layer perceptron composed of two linear projections and GeLU activation functions. The

experimental results are shown in Table 5.

Training Strategy. An optimized alternative to AS-BLO is AdamW, with parameters $b_1 = 0.9$, $b_2 = 0.999$, and weight decay is $1e - 4$. The ablation study of training strategies was performed on three tasks. Table. 6 showcases the enhancements achieved using our approximated sequential bi-level optimization approach relative to the direct joint training with our proposed EchoIR network. Our strategy posits that EchoIR should yield lossless image upsampling that is conducive to both human visual assessment and computational perception. By approximating the complex bi-level optimization into a sequence of single-level optimization tasks solvable by gradient descent, we reach a notably higher PSNR and SSIM.

Conclusion

In this paper, we propose the EchoIR model for various image restoration tasks. This model features an Echo-Upsampler, which utilizes encoder-provided feature maps for efficient upsampling despite poor input smoothness. To enhance feature extraction, we incorporate a Mix-Attention module. We employ the AS-BLO training strategy to fully train the Echo-Upsampler and achieve better reconstruction, optimizing the model during training. This strategy effectively models hierarchical tasks in image restoration and up-sampling. Experiments across multiple datasets and tasks show that our model achieves state-of-the-art performance in various image restoration tasks. **Broader Impacts.** EchoIR

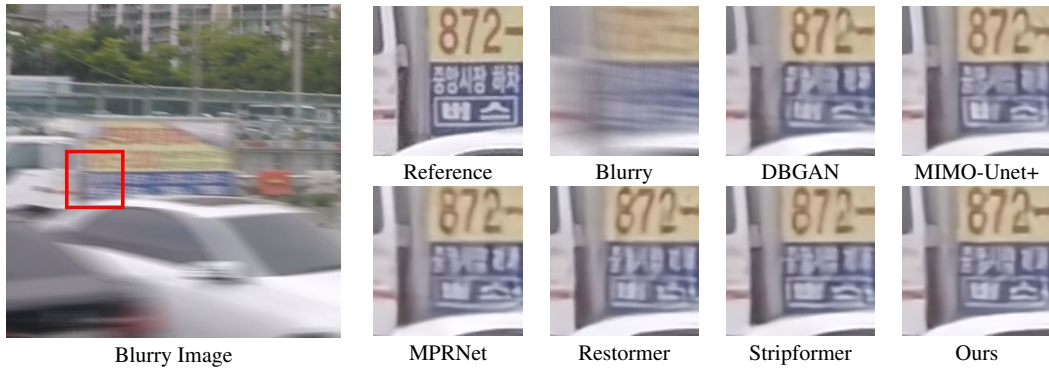


Figure 4: Visual comparison of the result with SOTA deblurring methods. This comparison employs the output results for direct comparison, thereby providing a clear reflection of the quality of the model’s output outcomes.

Table 3: Metrics comparison with the SOTA denoising methods. The best result is in red and the second best one is in blue. The compared methods include RIDNet (Anwar and Barnes 2019), VDN (Yue et al. 2019), SADNet (Chang et al. 2020), DANet+ (Yue et al. 2020), CycleISP (Zamir et al. 2020a), MIRNet (Zamir et al. 2020b), DreamNet (Ren et al. 2021), MPRNet, DAGL (Mou, Zhang, and Wu 2021), SwinIR, Uformer (Wang et al. 2022), Restormer, AirNet (Li et al. 2022a), and Burstormer.

Datasets	Metrics	RIDNet	VDN	SADNet	DANet+	CycleISP	MIRNet	DeamNet	MPRNet	DAGL	SwinIR	Uformer	Restormer	AirNet	Burstormer	EchoIR
SIDD	PSNR↑	38.71	39.28	39.46	39.47	39.52	39.72	39.47	39.71	38.94	39.81	39.77	39.91	39.95	39.93	40.05
	SSIM↑	0.951	0.956	0.957	0.957	0.957	0.959	0.957	0.958	0.953	0.958	0.959	0.958	0.958	0.958	0.962
DND	PSNR↑	39.26	39.38	39.59	39.58	39.56	39.88	39.63	39.80	39.77	39.91	39.96	39.97	39.99	39.96	40.06
	SSIM↑	0.953	0.952	0.952	0.955	0.956	0.956	0.953	0.954	0.956	0.955	0.956	0.956	0.955	0.955	0.960

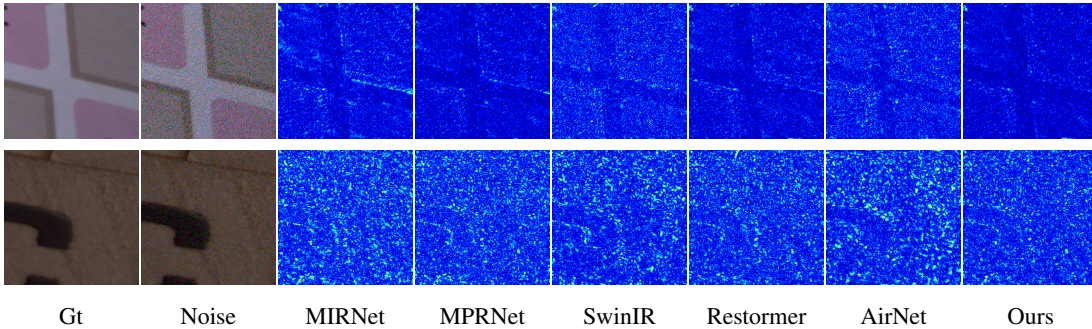


Figure 5: Visual comparison of the result with SOTA denoising methods. This comparison employs the difference map for clear comparison, thereby providing a clear reflection of the quality of the model’s output outcomes.

Table 4: Ablation study of Echo-Upsampler. PS stands for simple Pixel Shuffle method. TC stands for Transpose Convolution. EU stands for Echo-Upsampler referencing feature maps. The results are the average values of five test datasets.

Type	Params(M)	FLOPs(G)	PSNR	SSIM
PS	33,43	183.33	31.18	0.895
TC	30.25	178.69	31.24	0.901
EU	30.28	176.35	31.43	0.908

innovatively divides the entire process into the upper-layer image restoration task and the lower-layer upsampling task, and uses Approximated Sequential Bi-level Optimization for

Table 5: Ablation study of Mix-Attention Block. A check mark indicates that this structure is adopted.

CA	GDFN	Params(M)	FLOPs(G)	PSNR	SSIM
		13.12	85.43	36.35	0.930
	✓	22.98	176.31	39.53	0.953
✓		20.42	85.46	36.56	0.932
✓	✓	30.26	176.35	39.61	0.955

optimization. EchoIR provides a new paradigm for image restoration tasks.

Table 6: Ablation study of bi-level optimization strategy. SL is the single-level optimization strategy. The table displays the average PSNR of the Deraining, Deblurring, and Denoising tasks on different datasets

Type	FLOPs(G)	Derain	Deblur	Denoise
SL	171.41	31.21	30.25	39.36
AS-BLO	176.35	31.43	30.61	39.61

References

- Abdelhamed, A.; Lin, S.; and Brown, M. S. 2018. A high-quality denoising dataset for smartphone cameras. In *Proceedings of the IEEE conference on computer vision and pattern recognition*, 1692–1700.
- Anwar, S.; and Barnes, N. 2019. Real image denoising with feature attention. In *Proceedings of the IEEE/CVF international conference on computer vision*, 3155–3164.
- Cavigelli, L.; Hager, P.; and Benini, L. 2017. CAS-CNN: A deep convolutional neural network for image compression artifact suppression. In *2017 International Joint Conference on Neural Networks (IJCNN)*, 752–759.
- Chang, M.; Li, Q.; Feng, H.; and Xu, Z. 2020. Spatial-adaptive network for single image denoising. In *Computer Vision–ECCV 2020: 16th European Conference, Glasgow, UK, August 23–28, 2020, Proceedings, Part XXX 16*, 171–187. Springer.
- Chen, H.; Wang, Y.; Guo, T.; Xu, C.; Deng, Y.; Liu, Z.; Ma, S.; Xu, C.; Xu, C.; and Gao, W. 2021. Pre-Trained Image Processing Transformer. arXiv:2012.00364.
- Chen, X.; Wang, X.; Zhou, J.; Qiao, Y.; and Dong, C. 2023a. Activating More Pixels in Image Super-Resolution Transformer. In *Proceedings of the IEEE/CVF Conference on Computer Vision and Pattern Recognition (CVPR)*, 22367–22377.
- Chen, Z.; Zhang, Y.; Gu, J.; Kong, L.; and Yang, X. 2024. Recursive Generalization Transformer for Image Super-Resolution. In *ICLR*.
- Chen, Z.; Zhang, Y.; Gu, J.; Kong, L.; Yang, X.; and Yu, F. 2023b. Dual aggregation transformer for image super-resolution. In *Proceedings of the IEEE/CVF international conference on computer vision*, 12312–12321.
- Chen, Z.; Zhang, Y.; Gu, J.; Kong, L.; Yang, X.; and Yu, F. 2023c. Dual Aggregation Transformer for Image Super-Resolution. In *ICCV*.
- Cho, S.-J.; Ji, S.-W.; Hong, J.-P.; Jung, S.-W.; and Ko, S.-J. 2021. Rethinking coarse-to-fine approach in single image deblurring. In *Proceedings of the IEEE/CVF international conference on computer vision*, 4641–4650.
- Dong, C.; Loy, C. C.; He, K.; and Tang, X. 2014. Image Super-Resolution Using Deep Convolutional Networks. *IEEE Transactions on Pattern Analysis and Machine Intelligence*, 38.
- Dosovitskiy, A.; Beyer, L.; Kolesnikov, A.; Weissenborn, D.; Zhai, X.; Unterthiner, T.; Dehghani, M.; Minderer, M.; Heigold, G.; Gelly, S.; Uszkoreit, J.; and Hounsby, N. 2021. An Image is Worth 16x16 Words: Transformers for Image Recognition at Scale. *ICLR*.
- Dudhane, A.; Zamir, S. W.; Khan, S.; Khan, F. S.; and Yang, M.-H. 2023. Burstformer: Burst image restoration and enhancement transformer. In *2023 IEEE/CVF Conference on Computer Vision and Pattern Recognition (CVPR)*, 5703–5712. IEEE.
- Fu, X.; Huang, J.; Ding, X.; Liao, Y.; and Paisley, J. 2017a. Clearing the skies: A deep network architecture for single-image rain removal. *IEEE Transactions on Image Processing*, 26(6): 2944–2956.
- Fu, X.; Huang, J.; Zeng, D.; Huang, Y.; Ding, X.; and Paisley, J. 2017b. Removing rain from single images via a deep detail network. In *Proceedings of the IEEE conference on computer vision and pattern recognition*, 3855–3863.
- Gulrajani, I.; Ahmed, F.; Arjovsky, M.; Dumoulin, V.; and Courville, A. C. 2017. Improved Training of Wasserstein GANs. In Guyon, I.; Luxburg, U. V.; Bengio, S.; Wallach, H.; Fergus, R.; Vishwanathan, S.; and Garnett, R., eds., *Advances in Neural Information Processing Systems*, volume 30. Curran Associates, Inc.
- He, K.; Zhang, X.; Ren, S.; and Sun, J. 2016. Deep residual learning for image recognition. In *Proceedings of the IEEE conference on computer vision and pattern recognition*, 770–778.
- Jiang, K.; Wang, Z.; Yi, P.; Chen, C.; Huang, B.; Luo, Y.; Ma, J.; and Jiang, J. 2020. Multi-scale progressive fusion network for single image deraining. In *Proceedings of the IEEE/CVF conference on computer vision and pattern recognition*, 8346–8355.
- Jiang, Z.; Li, X.; Liu, J.; Fan, X.; and Liu, R. 2024. Towards Robust Image Stitching: An Adaptive Resistance Learning against Compatible Attacks. In *Proceedings of the AAAI Conference on Artificial Intelligence*, volume 38, 2589–2597.
- Kim, J.; Lee, J. K.; and Lee, K. M. 2016. Accurate Image Super-Resolution Using Very Deep Convolutional Networks. In *Proceedings of the IEEE Conference on Computer Vision and Pattern Recognition (CVPR)*.
- Kopf, J.; Cohen, M. F.; Lischinski, D.; and Uyttendaele, M. 2007. Joint bilateral upsampling. *ACM Transactions on Graphics (ToG)*, 26(3): 96–es.
- Kupyn, O.; Budzan, V.; Mykhailych, M.; Mishkin, D.; and Matas, J. 2018. Deblurgan: Blind motion deblurring using conditional adversarial networks. In *Proceedings of the IEEE conference on computer vision and pattern recognition*, 8183–8192.
- Kupyn, O.; Martyniuk, T.; Wu, J.; and Wang, Z. 2019. Deblurgan-v2: Deblurring (orders-of-magnitude) faster and better. In *Proceedings of the IEEE/CVF international conference on computer vision*, 8878–8887.
- LeCun, Y.; Bengio, Y.; and Hinton, G. 2015. Deep learning. *nature*, 521(7553): 436–444.
- Li, B.; Liu, X.; Hu, P.; Wu, Z.; Lv, J.; and Peng, X. 2022a. All-in-one image restoration for unknown corruption. In *Proceedings of the IEEE/CVF Conference on Computer Vision and Pattern Recognition*, 17452–17462.

- Li, W.; Lu, X.; Qian, S.; Lu, J.; Zhang, X.; and Jia, J. 2022b. On Efficient Transformer-Based Image Pre-training for Low-Level Vision. *arXiv:2112.10175*.
- Li, X.; Liu, J.; Chen, Z.; Zou, Y.; Ma, L.; Fan, X.; and Liu, R. 2025. Contourlet residual for prompt learning enhanced infrared image super-resolution. In *European Conference on Computer Vision*, 270–288. Springer.
- Li, X.; Zou, Y.; Liu, J.; Jiang, Z.; Ma, L.; Fan, X.; and Liu, R. 2023. From Text to Pixels: A Context-Aware Semantic Synergy Solution for Infrared and Visible Image Fusion. *arXiv preprint arXiv:2401.00421*.
- Liang, J.; Cao, J.; Sun, G.; Zhang, K.; Van Gool, L.; and Timofte, R. 2021. SwinIR: Image Restoration Using Swin Transformer. *arXiv preprint arXiv:2108.10257*.
- Mou, C.; Wang, Q.; and Zhang, J. 2022. Deep generalized unfolding networks for image restoration. In *Proceedings of the IEEE/CVF Conference on Computer Vision and Pattern Recognition*, 17399–17410.
- Mou, C.; Zhang, J.; and Wu, Z. 2021. Dynamic attentive graph learning for image restoration. In *Proceedings of the IEEE/CVF international conference on computer vision*, 4328–4337.
- Nah, S.; Hyun Kim, T.; and Mu Lee, K. 2017. Deep multi-scale convolutional neural network for dynamic scene deblurring. In *Proceedings of the IEEE conference on computer vision and pattern recognition*, 3883–3891.
- Park, D.; Kang, D. U.; Kim, J.; and Chun, S. Y. 2020. Multi-temporal recurrent neural networks for progressive non-uniform single image deblurring with incremental temporal training. In *European Conference on Computer Vision*, 327–343. Springer.
- Plotz, T.; and Roth, S. 2017. Benchmarking denoising algorithms with real photographs. In *Proceedings of the IEEE conference on computer vision and pattern recognition*, 1586–1595.
- Purohit, K.; Suin, M.; Rajagopalan, A.; and Boddeti, V. N. 2021. Spatially-adaptive image restoration using distortion-guided networks. In *Proceedings of the IEEE/CVF international conference on computer vision*, 2309–2319.
- Ren, C.; He, X.; Wang, C.; and Zhao, Z. 2021. Adaptive consistency prior based deep network for image denoising. In *Proceedings of the IEEE/CVF conference on computer vision and pattern recognition*, 8596–8606.
- Ren, D.; Zuo, W.; Hu, Q.; Zhu, P.; and Meng, D. 2019. Progressive image deraining networks: A better and simpler baseline. In *Proceedings of the IEEE/CVF conference on computer vision and pattern recognition*, 3937–3946.
- Rim, J.; Lee, H.; Won, J.; and Cho, S. 2020. Real-world blur dataset for learning and benchmarking deblurring algorithms. In *Computer Vision–ECCV 2020: 16th European Conference, Glasgow, UK, August 23–28, 2020, Proceedings, Part XXV 16*, 184–201. Springer.
- Ronneberger, O.; Fischer, P.; and Brox, T. 2015. U-net: Convolutional networks for biomedical image segmentation. In *Medical image computing and computer-assisted intervention–MICCAI 2015: 18th international conference, Munich, Germany, October 5–9, 2015, proceedings, part III 18*, 234–241. Springer.
- Shen, Z.; Wang, W.; Lu, X.; Shen, J.; Ling, H.; Xu, T.; and Shao, L. 2019. Human-aware motion deblurring. In *Proceedings of the IEEE/CVF International Conference on Computer Vision*, 5572–5581.
- Tao, X.; Gao, H.; Shen, X.; Wang, J.; and Jia, J. 2018. Scale-recurrent network for deep image deblurring. In *Proceedings of the IEEE conference on computer vision and pattern recognition*, 8174–8182.
- Tsai, F.-J.; Peng, Y.-T.; Lin, Y.-Y.; Tsai, C.-C.; and Lin, C.-W. 2022. Stripformer: Strip transformer for fast image deblurring. In *European Conference on Computer Vision*, 146–162. Springer.
- Vaswani, A.; Shazeer, N.; Parmar, N.; Uszkoreit, J.; Jones, L.; Gomez, A. N.; Kaiser, L. u.; and Polosukhin, I. 2017. Attention is All you Need. In Guyon, I.; Luxburg, U. V.; Bengio, S.; Wallach, H.; Fergus, R.; Vishwanathan, S.; and Garnett, R., eds., *Advances in Neural Information Processing Systems*, volume 30. Curran Associates, Inc.
- Wang, Q.; Jiang, K.; Wang, Z.; Ren, W.; Zhang, J.; and Lin, C.-W. 2023. Multi-scale fusion and decomposition network for single image deraining. *IEEE Transactions on Image Processing*, 33: 191–204.
- Wang, X.; Yu, K.; Wu, S.; Gu, J.; Liu, Y.; Dong, C.; Qiao, Y.; and Change Loy, C. 2018. ESRGAN: Enhanced Super-Resolution Generative Adversarial Networks. In *Proceedings of the European Conference on Computer Vision (ECCV) Workshops*.
- Wang, Z.; Cun, X.; Bao, J.; Zhou, W.; Liu, J.; and Li, H. 2022. Uformer: A General U-Shaped Transformer for Image Restoration. In *Proceedings of the IEEE/CVF Conference on Computer Vision and Pattern Recognition (CVPR)*, 17683–17693.
- Wei, W.; Meng, D.; Zhao, Q.; Xu, Z.; and Wu, Y. 2019. Semi-supervised transfer learning for image rain removal. In *Proceedings of the IEEE/CVF conference on computer vision and pattern recognition*, 3877–3886.
- Yang, W.; Tan, R. T.; Feng, J.; Liu, J.; Guo, Z.; and Yan, S. 2017. Deep joint rain detection and removal from a single image. In *Proceedings of the IEEE conference on computer vision and pattern recognition*, 1357–1366.
- Yu, K.; Dong, C.; Loy, C. C.; and Tang, X. 2016. Deep Convolution Networks for Compression Artifacts Reduction. *arXiv:1608.02778*.
- Yue, Z.; Yong, H.; Zhao, Q.; Meng, D.; and Zhang, L. 2019. Variational denoising network: Toward blind noise modeling and removal. *Advances in neural information processing systems*, 32.
- Yue, Z.; Zhao, Q.; Zhang, L.; and Meng, D. 2020. Dual adversarial network: Toward real-world noise removal and noise generation. In *Computer Vision–ECCV 2020: 16th European Conference, Glasgow, UK, August 23–28, 2020, Proceedings, Part X 16*, 41–58. Springer.
- Zamir, S. W.; Arora, A.; Khan, S.; Hayat, M.; Khan, F. S.; and Yang, M.-H. 2022. Restormer: Efficient transformer

for high-resolution image restoration. In *Proceedings of the IEEE/CVF conference on computer vision and pattern recognition*, 5728–5739.

Zamir, S. W.; Arora, A.; Khan, S.; Hayat, M.; Khan, F. S.; Yang, M.-H.; and Shao, L. 2020a. Cycleisp: Real image restoration via improved data synthesis. In *Proceedings of the IEEE/CVF conference on computer vision and pattern recognition*, 2696–2705.

Zamir, S. W.; Arora, A.; Khan, S.; Hayat, M.; Khan, F. S.; Yang, M.-H.; and Shao, L. 2020b. Learning enriched features for real image restoration and enhancement. In *Computer Vision—ECCV 2020: 16th European Conference, Glasgow, UK, August 23–28, 2020, Proceedings, Part XXV 16*, 492–511. Springer.

Zamir, S. W.; Arora, A.; Khan, S.; Hayat, M.; Khan, F. S.; Yang, M.-H.; and Shao, L. 2021. Multi-stage progressive image restoration. In *Proceedings of the IEEE/CVF conference on computer vision and pattern recognition*, 14821–14831.

Zhang, H.; Dai, Y.; Li, H.; and Koniusz, P. 2019. Deep stacked hierarchical multi-patch network for image deblurring. In *Proceedings of the IEEE/CVF conference on computer vision and pattern recognition*, 5978–5986.

Zhang, H.; and Patel, V. M. 2018. Density-aware single image de-raining using a multi-stream dense network. In *Proceedings of the IEEE conference on computer vision and pattern recognition*, 695–704.

Zhang, H.; Sindagi, V.; and Patel, V. M. 2019. Image de-raining using a conditional generative adversarial network. *IEEE transactions on circuits and systems for video technology*, 30(11): 3943–3956.

Zhang, K.; Li, Y.; Zuo, W.; Zhang, L.; Van Gool, L.; and Timofte, R. 2022a. Plug-and-Play Image Restoration With Deep Denoiser Prior. *IEEE Transactions on Pattern Analysis and Machine Intelligence*, 44(10): 6360–6376.

Zhang, K.; Luo, W.; Zhong, Y.; Ma, L.; Stenger, B.; Liu, W.; and Li, H. 2020. Deblurring by realistic blurring. In *Proceedings of the IEEE/CVF conference on computer vision and pattern recognition*, 2737–2746.

Zhang, X.; Zeng, H.; Guo, S.; and Zhang, L. 2022b. Efficient long-range attention network for image super-resolution. In *European Conference on Computer Vision*, 649–667. Springer.

Zou, Y.; Chen, Z.; Zhang, Z.; Li, X.; Ma, L.; Liu, J.; Wang, P.; and Zhang, Y. 2024a. Contourlet Refinement Gate Framework for Thermal Spectrum Distribution Regularized Infrared Image Super-Resolution. *arXiv preprint arXiv:2411.12530*.

Zou, Y.; Li, X.; Jiang, Z.; and Liu, J. 2024b. Enhancing Neural Radiance Fields with Adaptive Multi-Exposure Fusion: A Bilevel Optimization Approach for Novel View Synthesis. In *Proceedings of the AAAI Conference on Artificial Intelligence*, volume 38, 7882–7890.

Zuo, W.; Zhang, K.; and Zhang, L. 2018. *Convolutional Neural Networks for Image Denoising and Restoration*, 93–123. Cham: Springer International Publishing. ISBN 978-3-319-96029-6.